Case Studies in Construction Materials 23 (2025) e05363

Contents lists available at ScienceDirect

Case Studies in Construction Materials

journal homepage: www.elsevier.com/locate/cscm

Functional group selection and topological effects in concrete transport inhibitors: Nano-mechanisms and design principles

Chengbo Liu [a], Qiuju Li [a], Pan Wang [a], Yue Zhang [a], Xinpeng Wang [a], Dongshuai Hou [a], Cong Lu [b], Xiangming Zhou [c,*], Muhan Wang [a,c,**]

[a] Department of Civil Engineering, Qingdao University of Technology, Qingdao 266033, China
[b] School of Civil Engineering, Southeast University, Nanjing 211189, China
[c] Department of Civil and Environmental Engineering, Brunel University London, Uxbridge, Middlesex UB8 3PH, United Kingdom

ARTICLE INFO

Keywords:
Concrete durability
Transportation inhibitors
Nanoscale
Molecular design

ABSTRACT

Chloride ion (Cl^-) ingress significantly reduces the durability of reinforced concrete, particularly in marine environments, due to the high permeability of concrete pores. Concrete transportation inhibitors (CTIs) have emerged as a potential solution, yet their inhibition mechanisms remain unclear. In this study, molecular dynamics simulations and quantum chemical analyses are employed to elucidate the performance of surfactant-like CTIs. Results show that the enhancement of nanoscale interfacial tension (IFT) is central to reducing fluid transport. Among the tested structures, the Bola-type molecule with phosphonic acid head groups (B-PO_3^{2-}) demonstrates the strongest adsorption to calcium silicate hydrate (C-S-H), low self-aggregation, and an enlarged interaction area with water. These properties allow B-PO_3^{2-} to act as an effective nanoscale barrier to chloride penetration. This work provides a molecular-level framework for evaluating CTIs and offers design principles for next-generation concrete additives aimed at improving durability in aggressive environments.

1. Introduction

The long-term durability of concrete [1,2] in marine infrastructure remains a great challenge, as exposure to the aggressive marine environment substantially shortens the service life of reinforced concrete [3] compared to inland conditions [4]. This accelerated degradation undermines structural reliability [5], elevates the risk of premature failure, and incurs considerable maintenance and rehabilitation costs [6]. One of the primary deterioration mechanisms in marine settings is the ingress of chloride ions from seawater [7,8], which diffuse through the pore network of the cementitious matrix and accumulate at the steel-concrete interface. Upon reaching a critical threshold concentration, chloride ions destabilize the passive oxide layer that protects the embedded steel reinforcement, thereby initiating localized corrosion [9–11]. Chloride transport through concrete driven by diffusion, capillary suction, and permeation is therefore recognized as a critical factor governing the onset and propagation of reinforcement corrosion [12]. Consequently, the development of strategies to reduce chloride ion transportation [13], such as microstructural densification [14] or chemical binding within the matrix [15,16], is a central focus of current research aimed at enhancing the durability of concrete [17] in marine environments.

* Corresponding author.
** Corresponding author at: Department of Civil Engineering, Qingdao University of Technology, Qingdao 266033, China.
E-mail address: wangmuhan@qut.edu.cn (M. Wang).

https://doi.org/10.1016/j.cscm.2025.e05363
Received 29 August 2025; Received in revised form 17 September 2025; Accepted 28 September 2025
Available online 29 September 2025

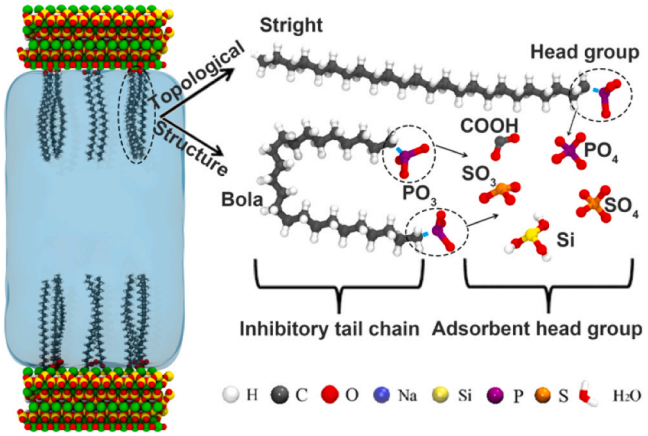

Fig. 1. Diagram of molecularly simulated pores and molecular models including hydrophobic topological species and head group adsorption functional groups; The white, gray, red, blue, yellow, purple and orange balls represent H, C, O, Na, Si, P and S atoms respectively.

There are several strategies currently employed for inhibiting chloride ion transportation in concrete, including the incorporation of mineral admixture [18–20], the application of surface coatings [21–23], and the techniques of electrochemical inhibition [24,25]. It is well established that cement mortars can effectively immobilize chloride ions and reduce their transportation within concrete by enhancing their adsorption capacity and forming stronger chemical bonds. In the study conducted by Wei et al. [20], the effects of various mineral admixtures on the chloride-binding capacity of cement mortar were investigated. The results indicated that the addition of fly ash and finely ground blast furnace slag significantly increased the chloride-binding rate in sulphoaluminate cement mortar, achieving increases of 46.6 % and 38.7 %, respectively. However, this approach presents challenges in practical engineering applications due to the complexities associated with mix ratio design and the variability in product properties [26]. Medeiros and Helen [21] examined the effectiveness of surface protection layers in preventing chloride penetration into concrete. Their findings revealed that all tested surface treatments significantly reduced the chloride adsorption rate by over 70 %, with polyurethane coatings achieving an impressive reduction rate of 86 %. Meanwhile, electrochemical inhibition represents a viable repair method that can effectively remove harmful substances, such as chloride ions, from concrete, thereby enhancing durability. Véronique et al. [24] reviewed previous research on electrochemical chloride extraction, a technique capable of treating corrosion induced by chlorides and repairing damaged structures. his method not only improves electrochemical properties but also enhances concrete durability. However, it also raises concerns regarding potential side effects and risks to concrete integrity. These studies can significantly inhibit the transportation of chloride ions in concrete, but the industrial manufacturing still hopes for a method that can be applied universally and is not limited to a specific system.

An alternative strategy involves the direct introduction of additives [27], which effectively prevents fluid ingress while providing a simple process and high cost-effectiveness [28–30].

Research on corrosion transportation inhibitors (CTIs) [31] has primarily focused on their capacity to mitigate ion transportation and improve the durability of cementitious materials [32]. Existing studies have examined the efficiency of different inhibitor types, molecular sizes, and topologies, yet investigations into the role of specific adsorbing functional groups remain scarce [33–36]. Our previous study [37] investigates and predicts the properties of corrosion transportation inhibitors (CTIs) featuring straight-chain and Bola-type topologies with different functional groups, while elucidating the interaction mechanisms between these inhibitors and calcium silicate hydrate (C-S-H). A deeper understanding of how functional groups govern inhibitor–substrate interactions is still lacking, limiting rational molecular design for optimal performance. This study applies molecular dynamics simulations to design CTIs with various functional groups as head groups and carbon chains as backbones. It investigates straight-chain and Bola-type topologies, elucidates their interaction with C-S-H, and compares inhibition efficiency across molecular morphologies. The results identify the Bola-type CTI with phosphonic acid (B-PO_3^{2-}) as the most competitive, enhancing interfacial tension by 15.8 % due to its dual strong adsorption groups and extended interaction area. These findings highlight the importance of functional groups in CTI design and provide guidance for developing more effective environmental inhibitors to enhance concrete durability.

2. Models and methods

2.1. Modelling details

In order to enhance the durability of C-S-H by modulating transportation with CTIs, two factors [33], the adsorption properties of CTIs on the C-S-H surface and the inhibition effect of the main chain topologies, play a crucial role. In the previous research on transportation inhibitors, it was found that most of the inhibitor structures on the market were straight chain structures (S), and the use of Bola-type (B) structures as the molecular topology could effectively improve the interfacial tension, thus improving the durability of concrete [37]. From the previous studies on superplasticizers [38], it is known that the functional groups with good adsorption

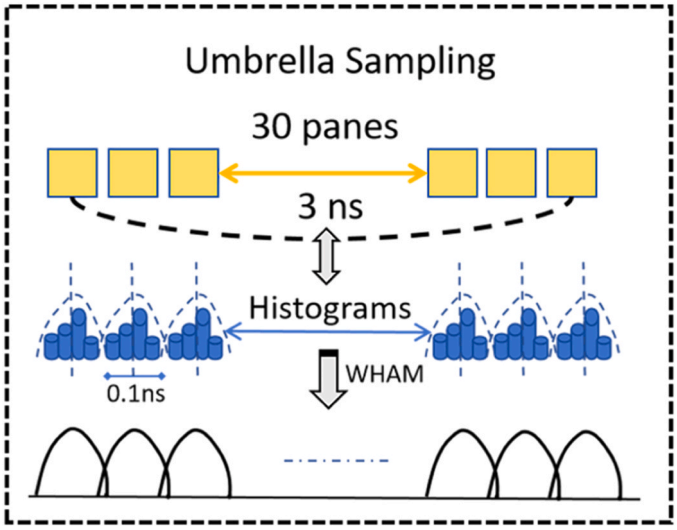

Fig. 2. Umbrella Sampling (US) diagram: Yellow indicates the sampling windows, blue traces the simulation pathway, and the black curve shows the reconstructed PMF.

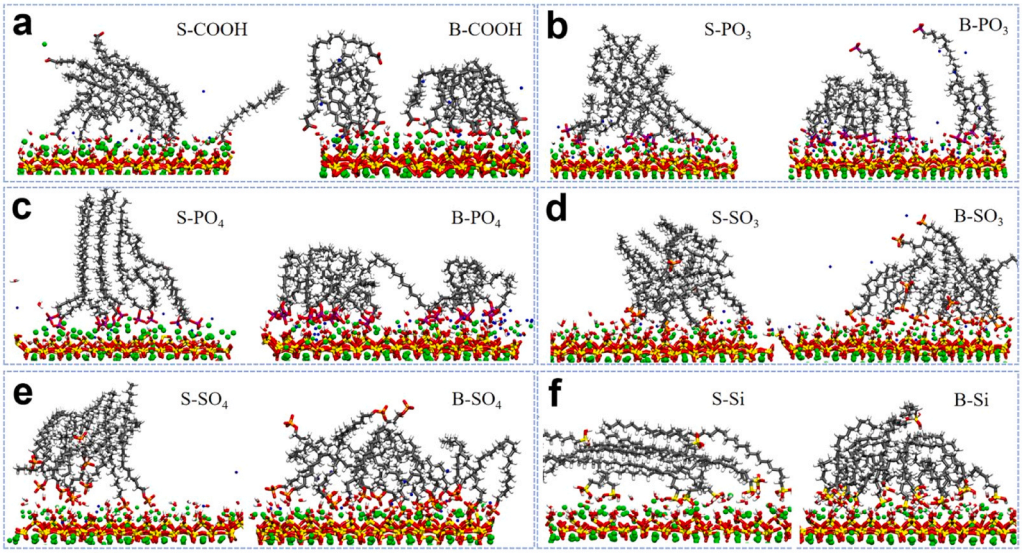

Fig. 3. (a−f) Stabilized adsorption phenomena in straight-chain and Bola-type structures featuring various adsorption functional groups.

properties include carboxyl (-COO^-), phosphonic acid (-PO_3^{2-}), phosphoric acid (-PO_4^{2-}), sulfonic acid (-SO_3^-), sulfuric acid (-SO_4^-), trimethylsilane (Si) and other adsorption functional groups [39,40].

In order to explore the effect of admixtures with different molecular structures on the transportation properties, twelve different molecular models were designed, as shown in Fig. 1. These models are distinguished based on the type of functional groups and different main chain topologies. Design by substitution of head group adsorption functional groups and hydrophobic alkane chain topology. The newly designed molecular structures follow the nomenclature of the International Union of Pure and Applied Chemistry (IUPAC) [41]. These are sodium tetracosanoate (S-COO^-), disodium tetracosanoate (B-COO^-), disodium tetracosylphosphonate (S-PO_3^{2-}), disodium {24-[bis (sodiooxy) phosphoxyl] tetracosyl} phosphonate (B-PO_3^{2-}), disodium tetracosyl phosphate (S-PO_4^{2-}), ({[(24-{[bis (sodiooxy) phosphoxyl] oxy}tetracosyl) oxy](sodiooxy) phosphoxyl} oxy)sodium (B-PO_4^{2-}), sodium tetracosane −1-sulfonate (S-SO_3^-), 1,24-disodium tetracosane-1,24-disulfonate (B-SO_3^-), sodium tetracosyl sulfate (S-SO_4^-), ({[(24-{[(sodiooxy)sulfonyl] oxy}tetracosyl)oxy]sulfonyl}oxy) sodium (B-SO_4^-), trimethoxy (tetracosyl)silane (S-Si), 3,3,28,28-tetxamethoxy-2,29-dioxa-3,28-disiltriacontane (B-Si).

The molecular modeling approach in this study adhered to the procedures established by Pellenq et al. [42] and Manzano et al. [43]. The initial unit cell adopted was a C-S-H structure measuring 11.16 Å × 7.39 Å × 22.77 Å, based on the model introduced by

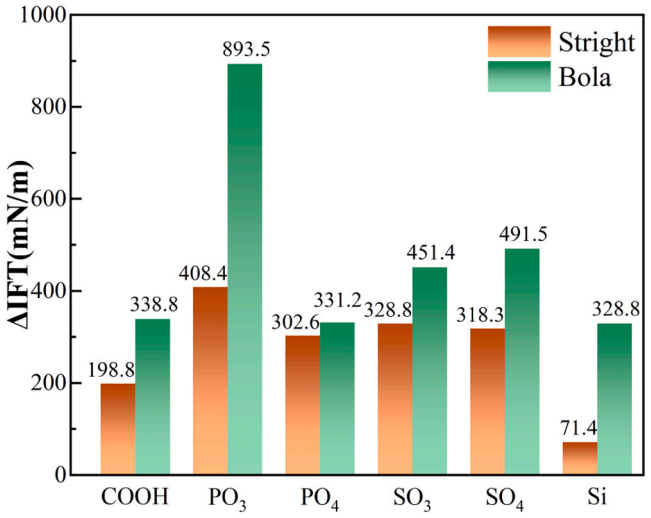

Fig. 4. The increase in interfacial tension (ΔIFT) for aqueous systems upon addition of CTI molecules.

Murray et al. [44]. To generate the final C-S-H configuration with enlarged cell parameters (44.64 Å × 44.34 Å × 45.54 Å, all angles 90°), a supercell was created through a 4 × 6 × 2 replication of the original unit cell along the three crystallographic axes. To maintain overall charge neutrality, surface non-bridging oxygen sites were passivated via hydroxylation [45], and selective deletion of surface calcium ions was carried out. This stabilized structure was then solvated in a periodic boundary box of dimensions 45.0 × 45.0 × 143.3 Å. To mimic the initial condition of concrete after admixture application, ten molecules of CTI were arranged on each of the top and bottom surfaces. Furthermore, to ensure a close-packed system, the number of water molecules was rounded up to 6600 from an initial estimate of 6330, which was derived by dividing the available box volume (189,945 $Å^3$) by the molecular volume of water (30 $Å^3$).

2.2. *Details of simulation*

2.2.1. *Force field*

Molecular Dynamics can overcome the limitations of static structural models and provide atomic-level dynamic descriptions of a system's behavior over time. This approach offers significant advantages for molecular-level design and computational studies. In our investigation, intermolecular interactions among CTI, water, and C-S-H substrates were modeled using the OPLS force field [46]. This choice was motivated by its renowned precision in molecular dynamics (MD) simulations [47,48] for complex systems. The OPLS (Optimized Potentials for Liquid Simulations) [49,50] potential, a foundational achievement in computational chemistry, was developed primarily by W.L. Jorgensen's [50] group at Ohio State University between the late 1980s and early 1990s. Its high fidelity stems from a careful optimization of atomic partial charges and van der Waals parameters, allowing it to accurately capture the properties and dynamics of diverse molecules. This methodological framework was instrumental in revealing the detailed mechanisms governing the interactions within our system. This study employs the OPLS-AA force field. It enables precise parameterization of organic molecules (including relevant functional groups) and reliably reproduces conformational behavior and thermodynamic properties.

2.2.2. *Classical molecular dynamics*

As an open-source molecular dynamics package from Sandia National Laboratories, LAMMPS [51] is engineered to simulate systems at atomic, molecular, and macromolecular scales. It serves as a powerful computational resource for investigating the dynamic evolution of diverse materials under various conditions. This flexibility has established it as an indispensable tool across numerous disciplines, including materials science, chemistry, and biochemistry.

All molecular dynamics (MD) simulations were performed in LAMMPS, leveraging the Nose-Hoover thermostat [52] to numerically integrate the equations of motion based on Hamiltonian dynamics [53], thereby ensuring consistent temperature regulation across the entire simulation. This method effectively maintains a constant temperature throughout the simulation. The simulation commenced with an NVT ensemble [54] phase, running for 0.1 ns at 1 K to fully optimize and equilibrate the initial configuration of the system. Following this phase, simulations are performed under the NPzT ensemble, where the temperature is held constant at 298 K and the pressure is maintained at one atmosphere in the Z direction for a duration of 1 ns to observe the system's behavior. The simulation was then extended for a further 5 ns within the same ensemble to promote structural equilibration and allow for the collection of sufficient data for statistical evaluation. During this phase, key thermodynamic parameters-including temperature, pressure, energy, and density-were logged every 100 time steps to support subsequent interpretation.

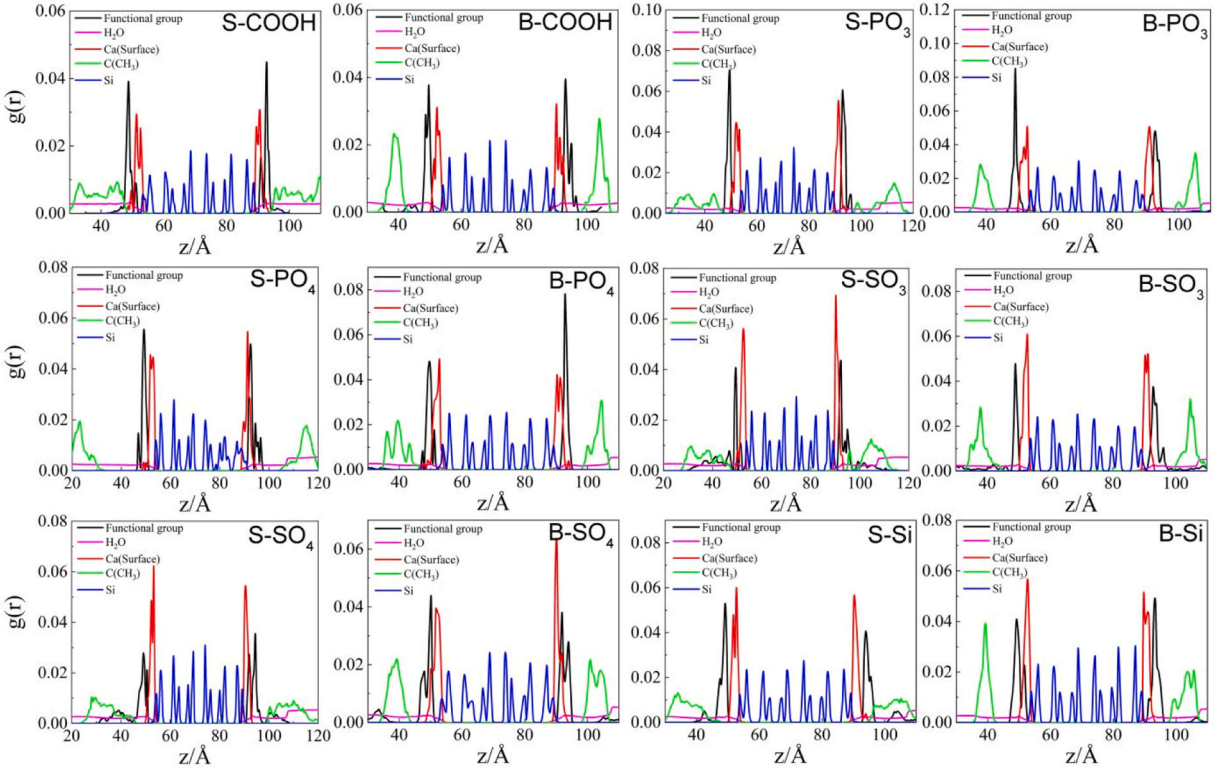

Fig. 5. One-dimensional density distribution curves of CTIs, the black, pink, red, and blue lines represent the distributions of Ca^{2+} on the surface of Functional group, H_2O, and C-S-H, and Si inside C-S-H, respectively. The green line $C_{(CH3)}$ represents the tail-chain C in the straight-chain type structure and the middle C in the Bola type structure.

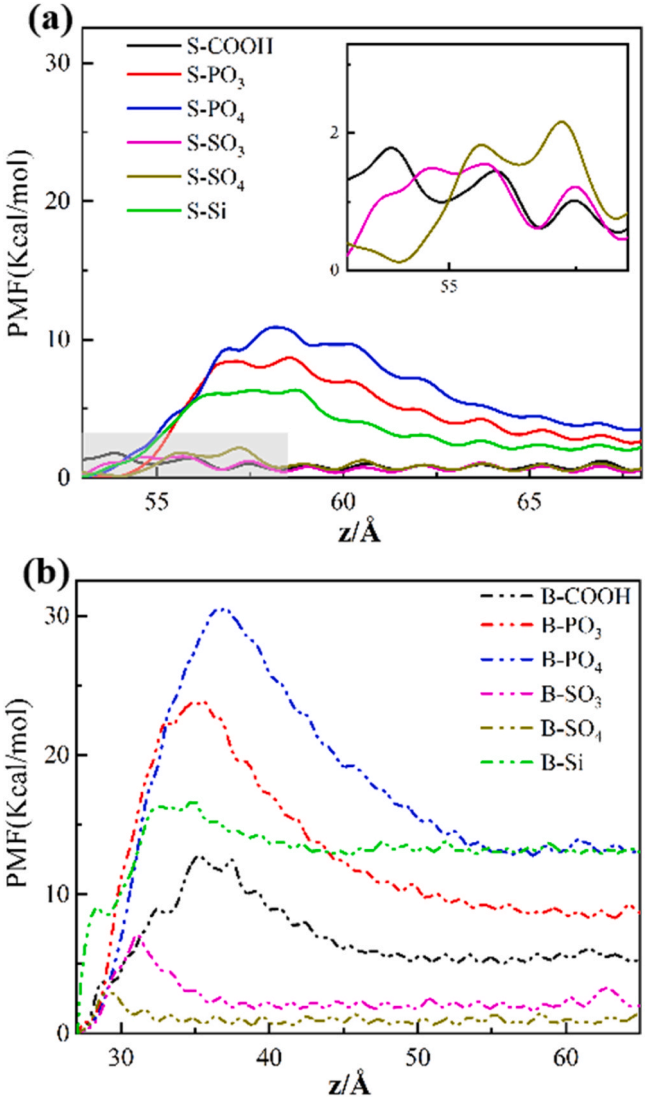

Fig. 6. (a) PMF with straight-chain structure (b) PMF with Bola structure.

2.3. Umbrella sample

Umbrella Sampling (US) [55,56] is a computational strategy widely used to determine the potential of mean force (PMF) across a reaction pathway. Unlike conventional molecular dynamics, which may insufficiently explore configurations separated by large energy barriers, US improves sampling efficiency by partitioning the reaction coordinate into discrete intervals, or "windows". Within each window, a harmonic biasing potential is applied to restrict the coordinate near a target value. Separate MD simulations are then run in these restrained windows, generating the statistical data required for reconstructing the free energy profile.

To reconstruct the complete PMF curve from the windowed sampling data, the weighted histogram analysis method (WHAM) [57, 58] is utilized. This approach effectively removes the bias introduced by the restraints, thereby recovering the true PMF. The PMF profile depicts the variation in free energy along the defined reaction coordinate, elucidating key molecular characteristics including energetically stable states and transition barriers. For this investigation, umbrella sampling was applied to twelve individual CTI molecules. Each molecule was simulated using a bias potential divided across 30 discrete windows at 298 K, with each window undergoing a 3 ns molecular dynamics simulation. (Fig. 2).

2.4. Quantum chemical calculations

The key molecular structures are modeled and quantum chemical calculations are performed by CP2K [59,60] to obtain the electronic structure after the simulation is completed. The key parts include the C-S-H surface Ca^{2+} and the partial structure of the head

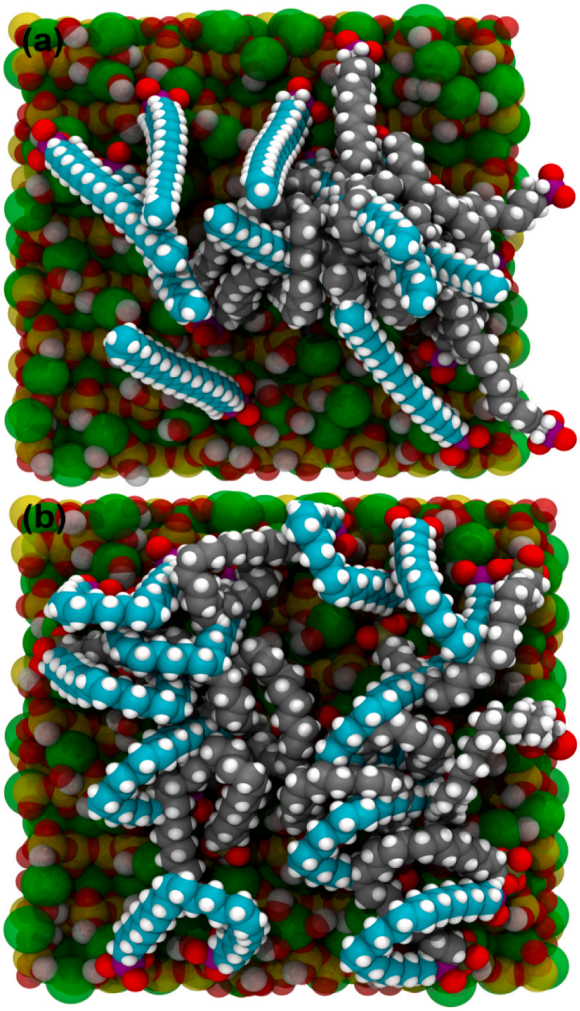

Fig. 7. (a) and (b) depict top views of S-PO_3^{2-} and B-PO_3^{2-}, respectively, with molecules colored cyan to denote the initial adsorption state and gray to signify the stable adsorption state.

Table 1
Percentage of area covered by CTIs calculated.

Type	-COO^-	-PO_3^{2-}	-PO_4^{2-}	-SO_3^-	-SO_4^-	Si
Stright	25.8 %	26.3 %	23.3 %	24.2 %	27.1 %	32.7 %
Bola	30.8 %	34.9 %	36.3 %	34.6 %	35.8 %	37.5 %

group functional group region of each molecule. The computationally generated wavefunction files were analyzed for electronic structure reduced density gradient (RDG) [61] and electron localization function (ELF) [62] using Multiwfn wavefunction analysis software [63]. RDG enables visualization and characterization of noncovalent interactions within systems, providing an intuitive representation of interaction types. ELF elucidates the localization properties of electron pairs and the nature of covalent bonds.

3. Results and discussion

3.1. Performance and structures

3.1.1. Stable structures

The adsorption properties of the molecular structure represent the initial step in understanding the stabilizing effects of CTIs and enhancing the durability of C-S-H. Consequently, investigating the adsorption behavior is essential. Upon reaching equilibrium in the kinetic simulations (Fig. 3), a representative configuration was chosen for each molecule to examine its adsorption characteristics after

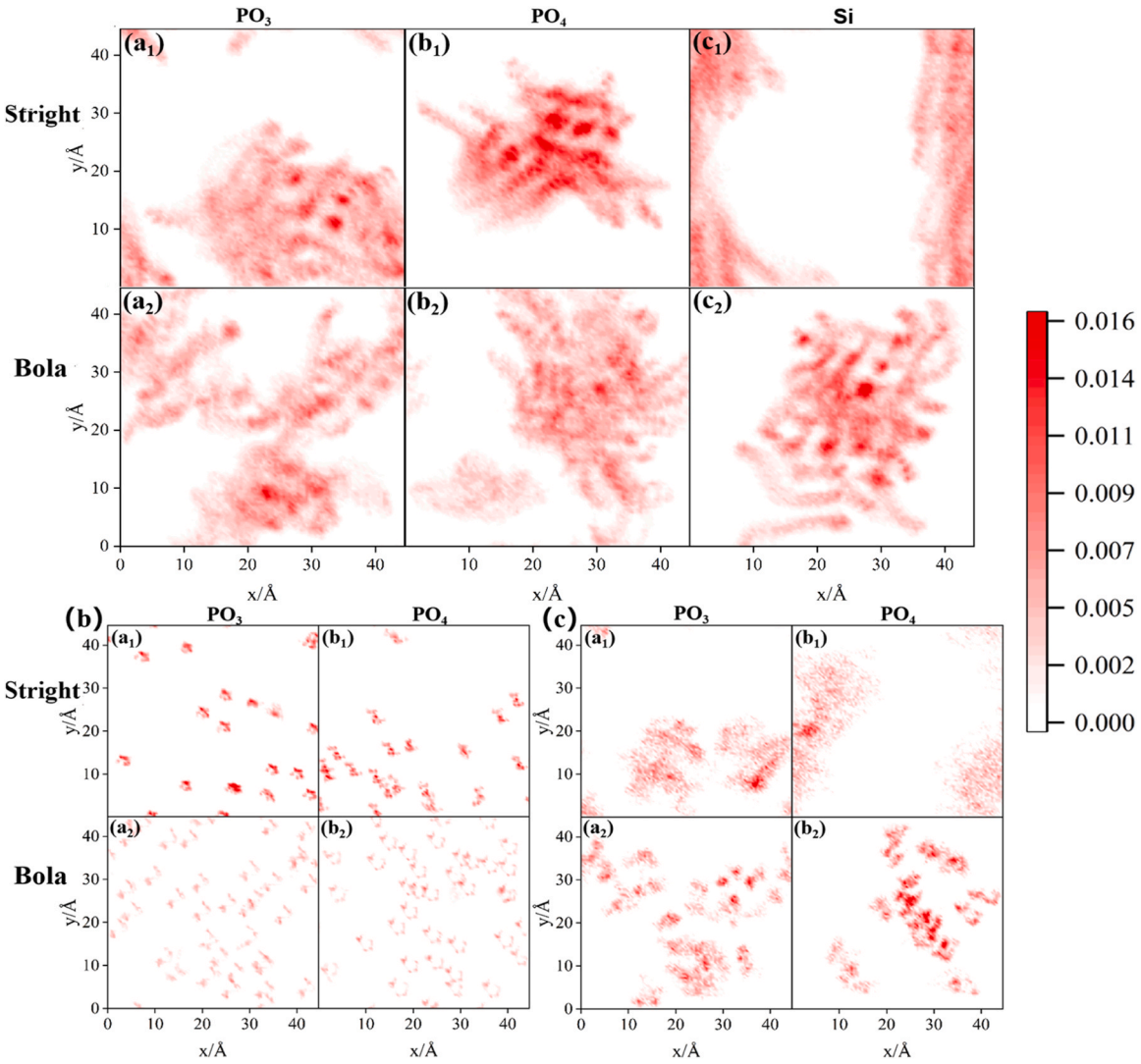

Fig. 8. (a) displays the two-dimensional density distribution of the main chain topology; (b) shows the two-dimensional density distribution of the head group; (c) illustrates the two-dimensional density distribution of the terminal carbon (C) in straight-chain types or the intermediate carbon (C) in Bola types. (a_1)-(c_1) represent -PO_3^{2-}, -PO_4^{2-}, Si in straight chain type and (a_2)-(c_2) represent -PO_3^{2-}, -PO_4^{2-}, Si in Bola type, respectively.

the stabilization phase.

All CTIs exhibit effective adsorption on the C-S-H surface. As shown in Fig. 3, Bola-type molecules adsorb closer to the surface than straight-chain types, indicating superior performance. This advantage arises from their dual head groups, which enhance interaction, while the shorter effective chain length does not compromise inhibition efficiency.

The adsorption orientations also differ between topologies: straight-chain molecules tend to align uniformly, whereas Bola-type molecules adopt a more random distribution. This dispersion is likely driven by the presence of two head groups, which reduce packing density but enlarge the effective contact area with water molecules, thereby influencing ion transportation. Functional group chemistry further modulates adsorption. For instance, S-Si shows poor adsorption and weak inhibition potential, whereas B-Si achieves markedly stronger adsorption. Notably, -$PO3^{2-}$ head groups consistently adsorb closest to the C-S-H surface, while -SO_3^- and -SO_4^- groups also display favorable performance. In summary, both molecular topology and functional groups strongly govern CTI adsorption behavior. These insights lay the groundwork for subsequent analyses of their mechanical, microstructural, and intermolecular effects on inhibition efficiency.

3.1.2. Relative interfacial tension

Interfacial tension (IFT) [64] serves as an indicator of the interfacial interactions between C-S-H surfaces and water, with elevated IFT values implying a diminished capacity for transportation. The calculated ΔIFT values (Fig. 4) were positive in all cases, confirming that the incorporation of CTIs effectively inhibits solution transportation.

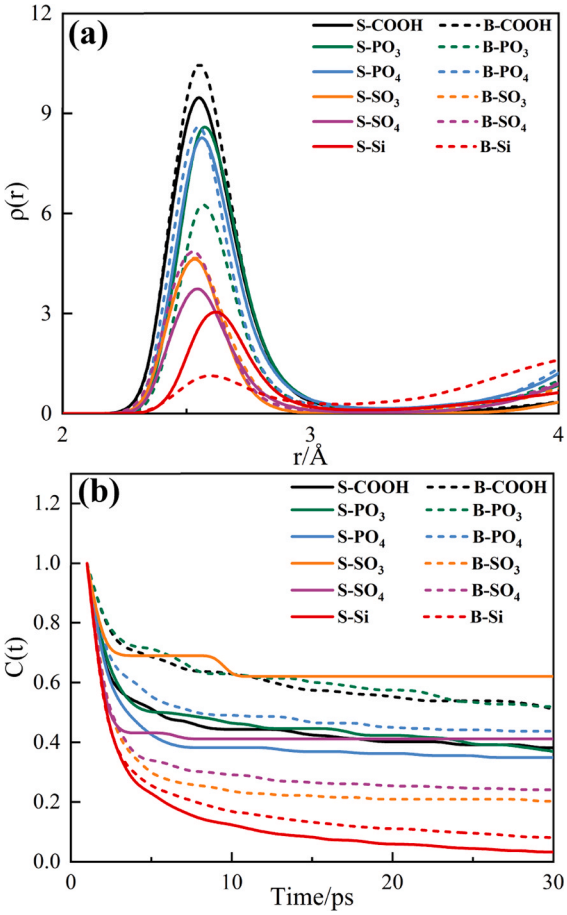

Fig. 9. a represents the RDF of oxygen in the head groups of CTIs with calcium on the C-S-H surface; b represents the TCF of oxygen in the head groups of CTIs with calcium on the C-S-H surface.

Table 2
BTE of CTIs during the last 1000 frames of their stable state.

Type		-COO^-	-PO_3^{2-}	-PO_4^{2-}	-SO_3^-	-SO_4^-	Si
Sum	Stright	30	46	52	18	19	55
	Bola	73	63	102	34	61	93
Average	Stright	30.72	47.39	52.44	18.17	19.77	57.25
	Bola	72.45	65.04	98.31	33.5	59.18	102.73

Bola-type inhibitors consistently outperformed straight-chain types, showing superior dispersion and enhanced inhibition. Among them, molecules with -PO_3^{2-} and Si head groups produced the most significant ΔIFT increases, consistent with their strong adsorption observed in Fig. 3. In particular, B-PO_3^{2-} achieved the highest ΔIFT, owing to its dual strong adsorption sites and effective molecular dispersion, which maximize transportation inhibition. By contrast, S-Si showed the weakest performance, with low ΔIFT values linked to poor adsorption and stronger disruption by water. For

-PO_4^{2-}-based inhibitors, the difference between Bola and straight-chain structures was minimal, likely because the high intrinsic adsorption strength of the -PO_4^{2-} group offsets head-group repulsion, resulting in only small changes in surface coverage. Both molecular topology and head-group chemistry critically determine the extent of transportation inhibition, with Bola-type structures—especially B-PO_3^{2-}—showing the most effective performance.

3.2. Micro-structural analysis

3.2.1. One-dimensional density distribution

To further examine nanoscale structural properties, Fig. 5 presents the one-dimensional density distribution [65] curves of the CTIs. Along the Z direction, the ranges of 50–52 Å and 90–92 Å correspond to the C-S-H adsorption surface, where functional groups

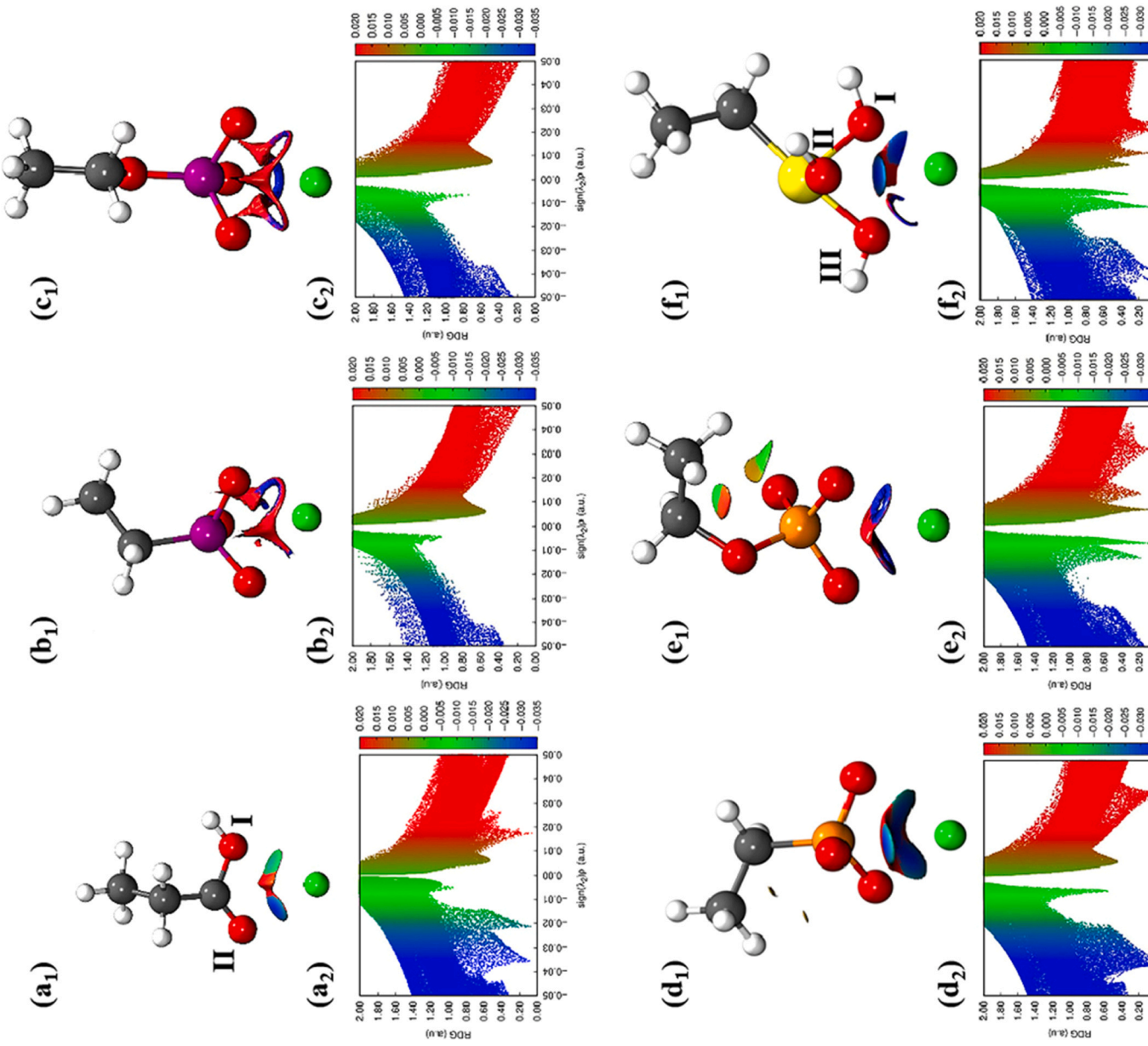
(a1)
(a2)
(b1)
(b2)
(c1)
(c2)
(d1)
(d2)
(e1)
(e2)
(f1)
(f2)
I
II
III
RDG (a.u)
sign(λ2)ρ (a.u.)

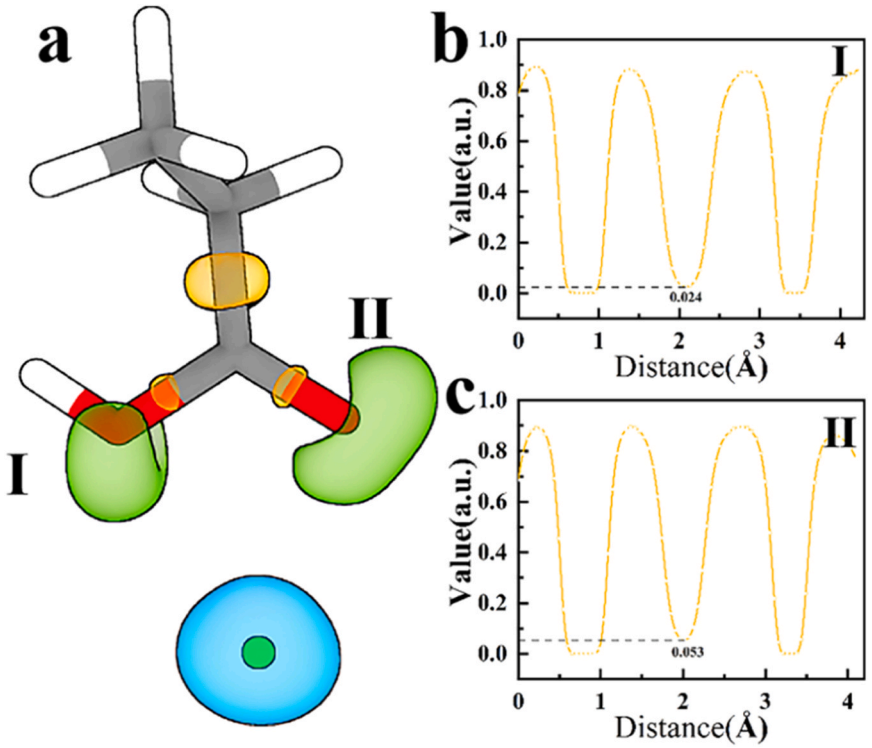

Fig. 11. ELF of Ca^{2+} on -COO^-, where (a) is the isosurface and (b,c) are the ELF curves for -COO^-. The blue and green colours represent the lone pair domains of Ca^{2+} and the core of oxygen atom, respectively. The values marked on the curves represent the ELF values at the time of interaction.

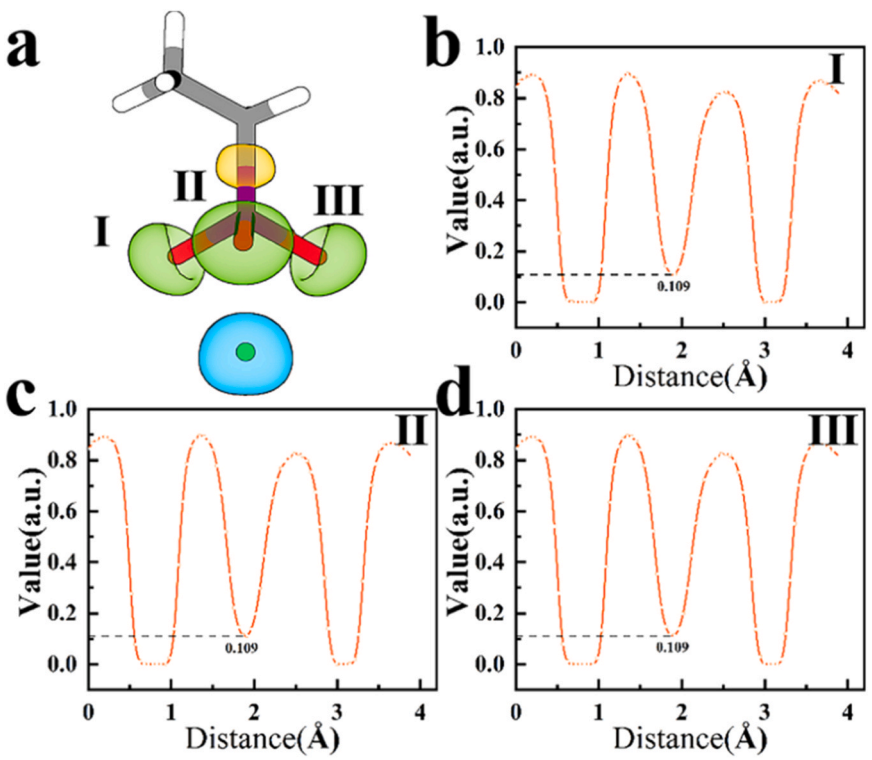

Fig. 12. ELF of Ca^{2+} on -PO_3^{2-}, where (a) is the isosurface and (b,c,d) are the ELF curves for -PO_3^{2-}. The blue and green colours represent the lone pair domains of Ca^{2+} and the core of oxygen atom, respectively. The values marked on the curves represent the ELF values at the time of interaction.

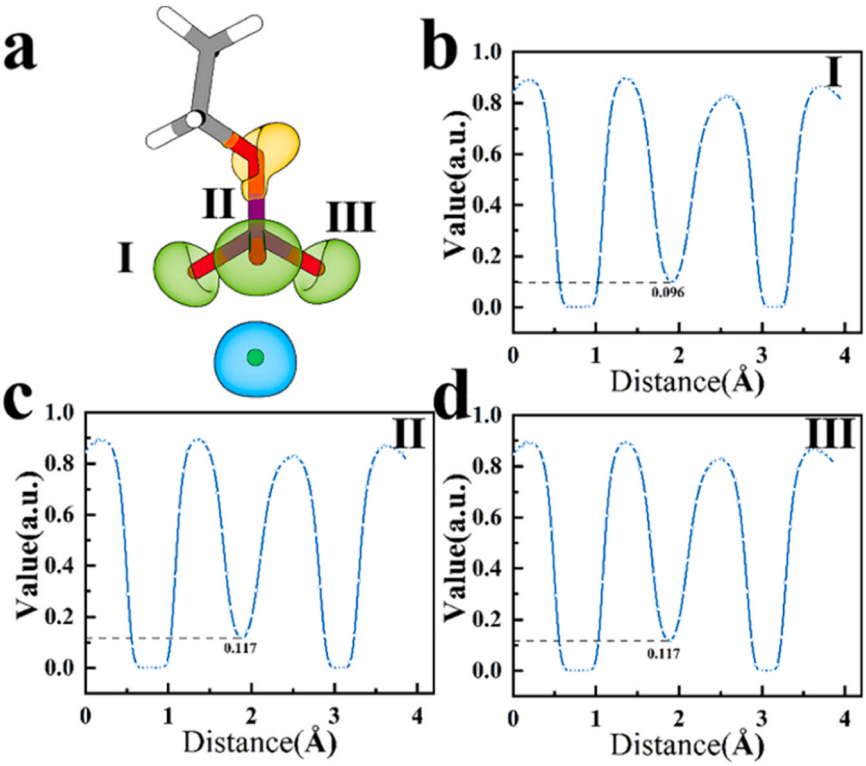

Fig. 13. ELF of Ca^{2+} on -PO_4^{2-}, where (a) is the isosurface and (b,c,d) are the ELF curves for -PO_4^{2-}. The blue and green colours represent the lone pair domains of Ca^{2+} and the core of oxygen atom, respectively. The values marked on the curves represent the ELF values at the time of interaction.

primarily interact with surface calcium atoms. Compared with straight-chain molecules, Bola-type structures display stronger overlap between functional groups and Ca^{2+}, resulting in more adsorption sites and enhanced surface binding.

Quantitatively, B-PO_3^{2-} shows the highest intersection value (0.03), whereas S-Si exhibits the lowest (<0.01), confirming B-PO_3^{2-} as the most effective and S-Si as the least effective inhibitor. Moreover, both -PO_3^{2-} and Si head groups in Bola-type structures achieve roughly double the adsorption capacity of their straight-chain counterparts, consistent with the adsorption patterns in Fig. 3 and the interfacial tension results in Fig. 4. Differences also emerge in the chain distribution. Straight-chain molecules show multiple peaks for tail carbons, reflecting flexible alkane chains that deform easily and distribute uniformly, but are also more susceptible to perturbation by water. In contrast, Bola-type molecules exhibit fewer, more concentrated peaks, indicating stiffer chains with reduced interaction with water molecules, thereby enhancing resistance to transportation.

Density distribution analysis reinforces that both molecular topology and functional groups critically shape adsorption behavior. Bola-type structures, particularly B-PO_3^{2-}, combine stronger adsorption with better resistance to water disturbance, which explains their superior inhibition performance observed across Figs. 3–5.

3.2.2. *Potential of mean force*

To further probe adsorption strength, the umbrella sampling (US) method was applied along the Z-axis to simulate molecular pullout and calculate potential of mean force (PMF) [66] curves (Fig. 6). The PMF profile starts at the lowest free-energy point, corresponding to the most stable adsorption state, while subsequent peaks represent energy barriers that must be overcome during desorption. The depth of the potential well and the magnitude of the energy drop reflect the stability of adsorption and the strength of molecular binding.

As shown in Fig. 6, Bola-type molecules display deeper potential wells and larger energy drops compared to straight-chain molecules, confirming their stronger adsorption capacity. Among them, B-PO_3^{2-} and B-PO_4^{2-} exhibit the most pronounced decreases, consistent with their superior adsorption observed in Fig. 3. By contrast, although B-Si shows a higher energy barrier, its relatively small energy drop indicates weaker adsorption. This suggests that the enhanced inhibition of B-Si arises more from the structural characteristics of the Bola-type topology than from the intrinsic adsorption of its head group.

3.2.3. *Coverage area calculation*

Fig. 7 shows that straight-chain molecules undergo aggregation upon stable adsorption, while Bola-type molecules retain their initial adsorption configuration with minimal change, maintaining their contact area with water as they do not self-aggregate.

To more intuitively illustrate the extent of the area covered by different molecular models, the area ratios of the molecules

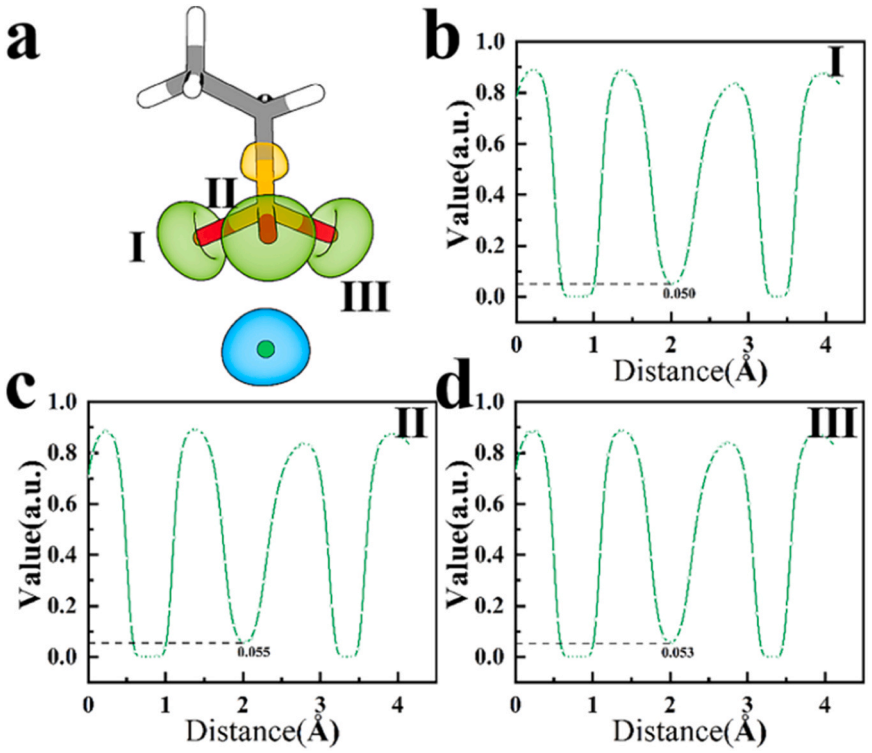

Fig. 14. ELF of Ca^{2+} on -SO_3^-, where (a) is the isosurface and (b,c,d) are the ELF curves for -SO_3^-. The blue and green colours represent the lone pair domains of Ca^{2+} and the core of oxygen atom, respectively. The values marked on the curves represent the ELF values at the time of interaction.

(represented by gray molecular chains) to the C-S-H surface at the stable adsorption state were calculated to obtain the results for Table 1**.** It is evident that all CTIs exhibit an increased coverage area for Bola-type structures compared to straight-chain types. This indicates a greater interaction area with water, which enhances their ability to inhibit transportation.

3.2.4. Two-dimensional density distribution

Calculations from the coverage area alone may be subject to error. In order to more accurately assess the mechanism of action, we calculated two-dimensional density distributions [67] in the X- and Y-plane directions (Fig. 8). Notably, there is little difference between the distributions of S-PO_4^{2-} and B-PO_4^{2-}, resulting in similar transportation inhibition effects. In contrast, the distributions of the other CTIs show significant differences, with Si exhibiting the most pronounced change. This observation aligns closely with the results related to interfacial tension presented in Fig. 4.

Bola-type molecules show a uniform distribution of head groups that closely matches their main chain distribution, whereas straight-chain molecules display a denser but less consistent head-group arrangement. This indicates that Bola-type structures provide a broader range of adsorption sites and a larger effective coverage area, while straight-chain molecules, with their more flexible topology, are easily perturbed by water. Fig. 8**c** further supports this distinction: the darker regions of the Bola-type structures reflect a concentrated distribution of intermediate carbons, highlighting their rigidity and reduced sensitivity to water. In contrast, the dispersed terminal carbons of straight-chain molecules reveal stronger water influence and greater conformational flexibility. When considered together with Fig. 8**b**, the correspondence between head-group and terminal-carbon distributions suggests that Bola-type molecules are more strongly anchored to the surface.

These observations are consistent with the adsorption patterns in Fig. 3 and the interfacial tension results in Fig. 4, providing additional evidence that the wider coverage and stronger resistance to water of Bola-type CTIs underpin their superior inhibition performance.

3.3. Interaction mechanism

To thoroughly investigate the mechanism of intermolecular interactions, we conducted radial distribution function (RDF) [68] calculations for calcium on the C-S-H surface in CTIs and for oxygen on the head groups of CTIs (Fig. 9**a**). It is evident that the peaks for Bola-type structures are higher than those for straight-chain types across all CTIs, except for -PO_3^{2-} and Si, within a radius of 2.7 Å. This indicates that the anchored adsorption strength of Bola-type structures is greater. Conversely, the lower values observed for -PO_3^{2-} and Si suggest a more dispersed distribution of their Bola-type head groups, resulting in more homogeneous adsorption and a larger contact area with water. This finding aligns with the interfacial tension results presented in Fig. 4.

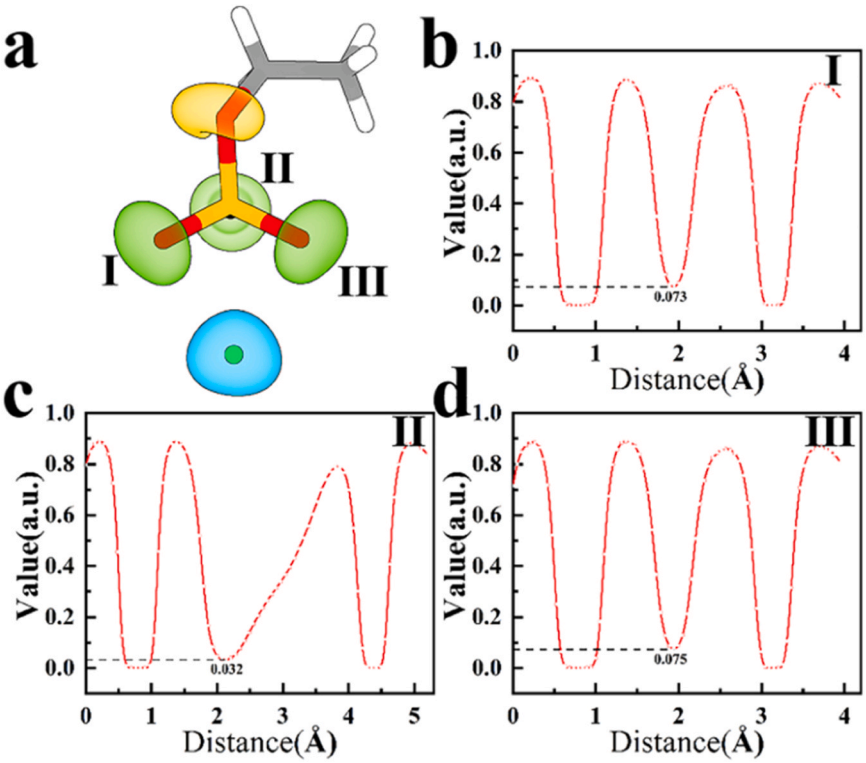

Fig. 15. ELF of Ca^{2+} on $-SO_4^-$, where (a) is the isosurface and (b,c,d) are the ELF curves for $-SO_4^-$. The blue and green colours represent the lone pair domains of Ca^{2+} and the core of oxygen atom, respectively. The values marked on the curves represent the ELF values at the time of interaction.

Fig. 9**b** present the time correlation function (TCF) [69] analyses. It is evident that the Bola-type curves for $-PO_3^{2-}$ and $-PO_4^{2-}$ exhibit a trend of rapid stabilization following a steady decline, indicating that their bond energies are sufficient and their adsorption performance is favorable, which corresponds to the conclusions drawn from the PMF in Fig. 6. In contrast, Si shows a continuous rapid decline, suggesting insufficient bond strength. Notably, B-PO_3^{2-} demonstrates the strongest bond energy and also exhibits good adsorption performance, aligning with the findings presented in Fig. 4.

We calculated the total number of bond interactions and the average number of bonds for CTIs during the last 1000 frames of their stable state, as shown in Table 2. It is evident that both the total number and the average for Bola-type molecules are higher than those for straight-chain types, indicating greater stability for Bola-type structures. Notably, B-Si shows a significant discrepancy between its total and average values, suggesting considerable fluctuations and instability in its bond interactions.

To further assess the adsorption characteristics of CTIs, quantum chemical calculations were performed on the head groups of each molecule in interaction with Ca^{2+} on the C-S-H surface, using the Multiwfn analysis package. RDG and ELF analyses were conducted to visualize weak interactions and to evaluate their nature. In the RDG isosurfaces and scatter plots (Fig. 10**a–f**), red, green, and blue regions represent steric effects, van der Waals (vdW) interactions, and electrostatic interactions, respectively. The results show that $-COO^-$ (Fig. 10**a**) interacts with Ca^{2+} mainly through vdW forces (–0.022) and electrostatics (–0.036), with no evidence of chemical bonding, confirming purely physical adsorption. Similarly, $-SO_3^-$ (Fig. 10**d**) exhibits three electrostatic interactions (–0.035) via its oxygen atoms, again without chemical bonding. In contrast, Si (Fig. 10**f**) shows a mixed behavior: two oxygens form electrostatic interactions (–0.04), while a third generates a ring-shaped isosurface indicative of weak chemical bonding, suggesting a combined physical–chemical adsorption process. Notably, $-PO_3^{2-}$, $-PO_4^{2-}$, and $-SO_4^-$ (Fig. 10**b, c, e**) all produce annular isosurfaces with inner blue and outer red rings, characteristic of weak bonding interactions and stronger adsorption capacity.

Taken together, these results indicate that while $-COO^-$ and $-SO_3^-$ rely on weaker physical adsorption, groups such as $-PO_3^{2-}$, $-PO_4^{2-}$, $-SO_4^-$, and partly Si engage in weak chemical bonding, thereby offering more robust interaction with Ca^{2+} and enhanced adsorption strength.

While RDG analysis provides a qualitative view of the interaction types, it does not capture the strength of adsorption between functional groups and Ca^{2+}. To address this, Electron Localization Function (ELF) analysis was performed. ELF is a three-dimensional real-space function ranging from 0 to 1, which reveals electron localization, lone pairs, and the nature of chemical bonding. Regions of high ELF indicate tightly bound electrons and stronger binding, while low ELF reflects weaker electron confinement and easier electron mobility.

Figs. 11–16 present the local electronic structures of Ca^{2+} adsorbed on different functional groups. In each figure, the a-plots show the isosurfaces, and the remaining plots depict ELF values. The four apical peaks in the ELF plots correspond, from left to right, to:

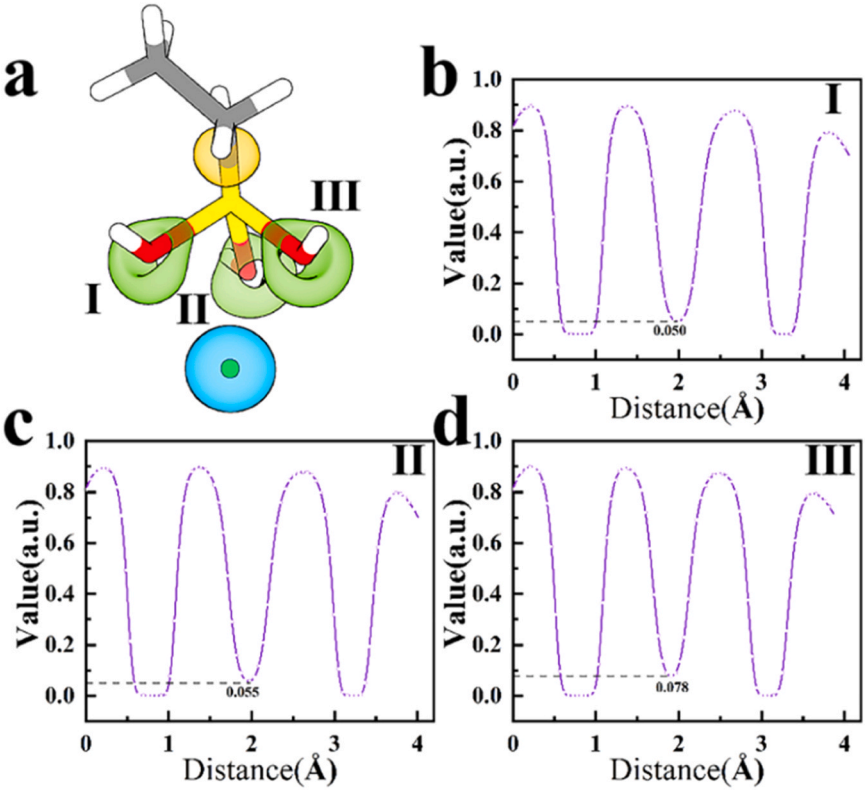

Fig. 16. ELF of Ca^{2+} on Si, where (a) is the isosurface and (b,c,d) are the ELF curves for Si. The blue and green colours represent the lone pair domains of Ca^{2+} and the core of oxygen atom, respectively. The values marked on the curves represent the ELF values at the time of interaction.

electrons of Ca^{2+}, electrons shared by Ca^{2+} in Ca-O pairs, electrons contributed by oxygen in Ca-O pairs, and the oxygen electrons themselves. Across all functional groups, Ca^{2+} consistently forms covalent interactions with oxygen atoms, in agreement with the atom-level interactions shown in Fig. 5.

Specifically, in $-COO^-$ (Fig. 11), oxygen atom II dominates the interaction (ELF = 0.053 vs. 0.024 for atom I). In $-PO_4^{2-}$ (Fig. 13), oxygen atoms II and III are the primary contributors, while in $-SO_4^-$ (Fig. 15), atoms I and III play major roles. For Si (Fig. 16), oxygen atom III is the main contributor. In contrast, $-PO_3^{2-}$ and $-SO_3^-$ (Figs. 12 and 14) show similar ELF values across all oxygen atoms ($-PO_3^{2-} \approx 0.109$, $-SO_3^- \approx 0.05$), indicating that the three oxygens jointly participate in adsorption.

Based on overall ELF analysis, the adsorption strength of functional groups to Ca^{2+} follows the order: $-PO_4^{2-} > -PO_3^{2-} > > -SO_4^- \approx$ Si $> -SO_3^- \approx -COO^-$. This ranking highlights that $-PO_4^{2-}$ and $-PO_3^{2-}$ provide the strongest interactions, followed by $-SO_4^-$ and Si, whereas $-SO_3^-$ and $-COO^-$ exhibit weaker adsorption. These trends are consistent with the molecule–surface adsorption distances observed in Fig. 3.

In the investigation of adsorption properties, it was observed that $-PO_3^{2-}$ and $-PO_4^{2-}$, which exhibit the best adsorption characteristics, produced contrasting results in the ΔIFT calculations presented in Fig. 3. Specifically, the increase in ΔIFT for B-PO_4^{2-} was less pronounced compared to that of B-PO_3^{2-}. This discrepancy may suggest that the enhanced adsorption performance of $-PO_4^{2-}$ influences the ability of the Bola-type structure to increase the effective area. Further investigation is warranted to explore this phenomenon. To further investigate the reasons behind the larger effective area of Bola-type structures, we performed RDF calculations on the head groups themselves during the simulation process (Fig. 17) to validate the self-aggregation capability of the CTIs.

A lower peak value and a gentler slope in the curves indicate poorer self-aggregation capability, which correlates with a larger interaction area with water, thereby enhancing the suppression of transportation effects. Conversely, a higher peak and steeper slope suggest less effective suppression. In Fig. 17, it is clear that although the number of head groups of the Bola-type molecule is twice that of the straight-chain molecule, the peak of the Bola-type molecule is less than twice that of the straight-chain molecule, and the curve is flatter. This indicates that Bola-type molecules have weaker self-aggregation capabilities but exhibit better suppression effects.

Additionally, in Fig. 17**a**, both structures of $-PO_4^{2-}$ show a broad distribution, suggesting similar suppression effects. The B-PO_3^{2-} peak is not only lower than that of the straight-chain type, but also more uniformly distributed, which suggests that it is less capable of self-aggregation and the transportation inhibition effect is more pronounced, and the same conclusion is found for B-Si in Fig. 17**b**. These conclusions align well with the results regarding IFT presented in Fig. 4.

To further investigate the self-aggregation capability of CTIs and the underlying reasons for this phenomenon, we placed the CTI molecules individually in a water box and conducted a 10 ns simulation to observe their natural state (Fig. 18**a**). Taking B-PO_3^{2-} as an example, after 10 ns, the distance between the head groups increased from 7.78 Å to 24.42 Å, indicating a tendency towards an

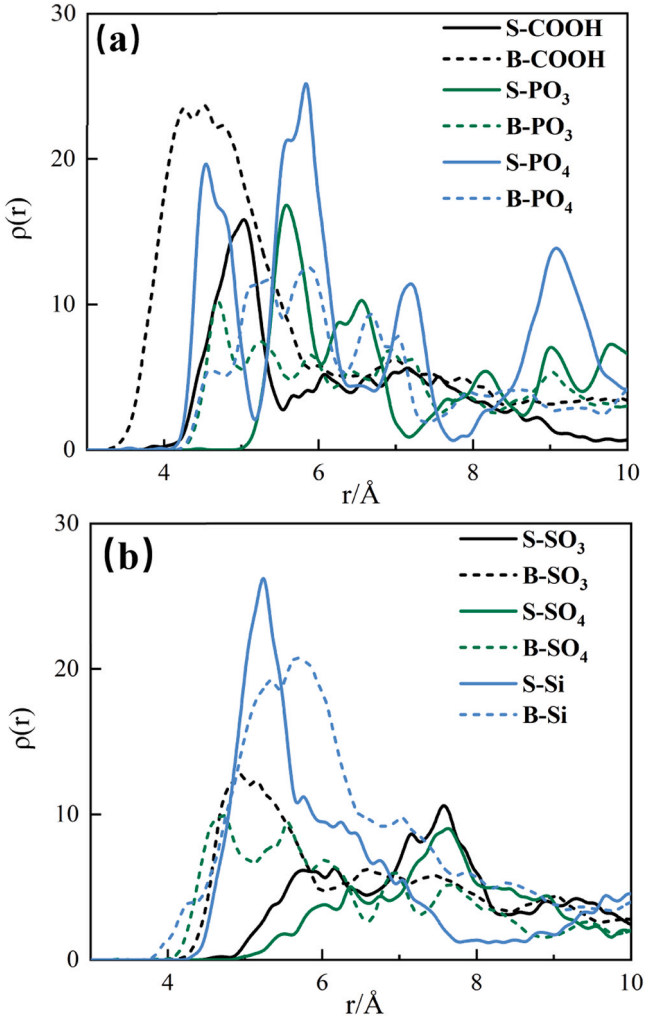

Fig. 17. RDF calculations between the head groups of CTIs to verify their self-aggregation capability. (a) represents the straight-chain and Bola-type structures with $-COO^-$, $-PO_3^{2-}$, and $-PO_4^{2-}$ as the head groups. (b) represents the straight-chain and Bola-type structures with $-SO_3^-$, $-SO_4^-$, and Si as the head groups.

elongated state. Similar results were observed for other Bola-type structures. Additionally, we calculated the average bond length over 1000 frames after the system reached stability (Fig. 18**b**). Further calculations confirmed that all Bola-type molecules tend to elongate in their natural state, demonstrating poor self-aggregation capability. This characteristic facilitates the formation of more distant adsorption sites on the C-S-H surface, thereby increasing the effective area of their topology and enhancing resistance to transportation. Notably, S-Si tends to bend while B-Si tends to elongate, suggesting a repulsive interaction between the two head groups of a Bola-type structure, thereby extending the topology. This is a primary reason for the poor self-aggregation capability and effective transportation suppression of Bola-type structures. This analysis also further indicates that the adsorption interaction between $-PO_4^{2-}$ and Ca^{2+} is stronger than the repulsive interactions between the head groups, leading to stable adsorption without significant elongation. Consequently, the changes in self-aggregation capability are minimal, resulting in the IFT outcomes observed in Fig. 4.

For evaluating the stability of CTIs' effects, the root mean square displacement (RMSD) [70,71] was calculated over the last 1000 frames to assess their variations and stability (Fig. 19). RMSD serves as a key metric for evaluating the average structural deviation of a molecule relative to its reference conformation during simulation, thereby reflecting its structural stability and conformational flexibility.

As shown in Fig. 19, the Bola-type structures exhibit lower values than their corresponding straight-chain structures, indicating a higher structural similarity and greater stability in their effects. It is evident that S-Si and B-Si differ significantly, indicating a substantial change in stability. In contrast, $-PO_3^{2-}$ and $-PO_4^{2-}$ show only minor differences, suggesting that both are relatively stable in their effects. This observation aligns with previous conclusions.

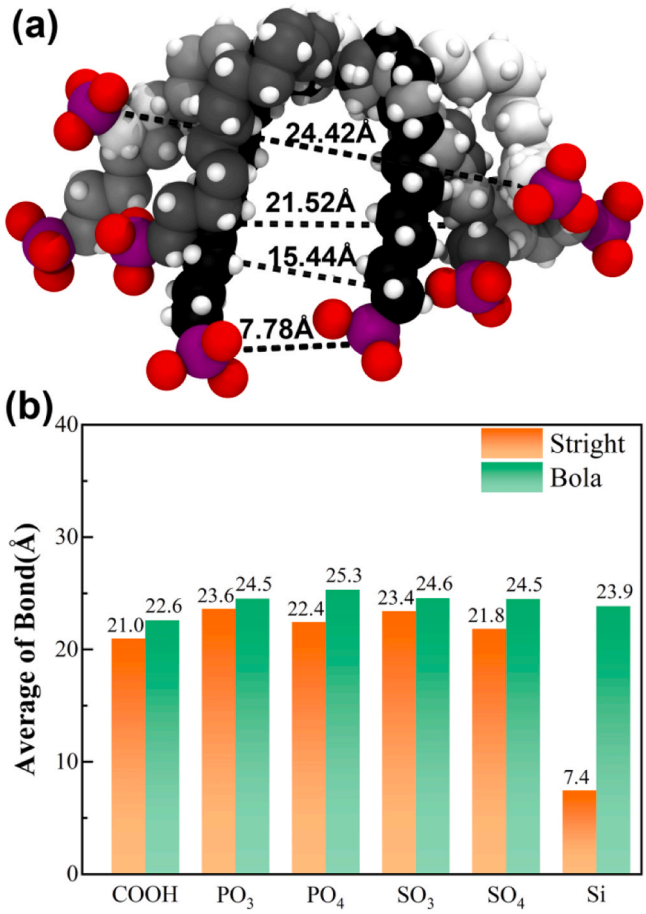

Fig. 18. (a) provides a schematic representation of the structural tendencies in the natural state, using B-PO_3^{2-} as an example. Color change from dark to light is the direction of structural change. The measured data represent the distance between head groups; (b) shows the calculation of the average chain length of CTIs based on the last 1000 frames in their natural state.

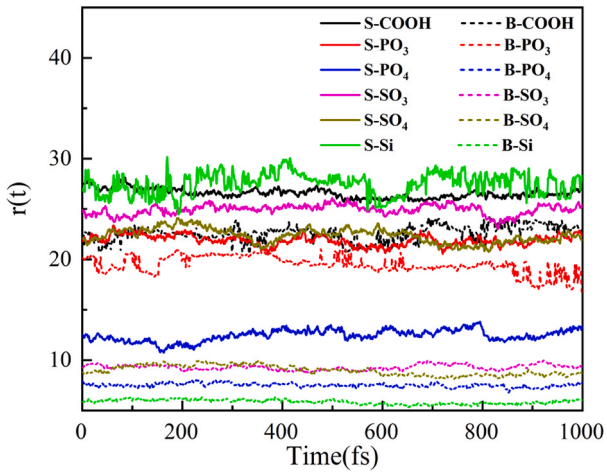

Fig. 19. Root mean square displacement analysis of CTIs.

4. Conclusion

This study sheds light on the mechanism by which surfactant-like concrete transportation inhibitors (CTIs) suppress chloride ion transportation in reinforced concrete. Combining molecular dynamics simulations and quantum chemical calculations, the results show that Bola-type molecules substantially enhance nanoscale interfacial tension (IFT). Among the functional groups tested, -PO_3^{2-} provides strong adsorption without interfering with repulsive interactions, and B-PO_3^{2-} emerges as the optimal structure, effectively acting as a barrier to fluid transportation. The findings highlight the critical roles of adsorption groups and molecular topology in optimizing CTI performance, offering guidance for the molecular design of concrete additives.

(1) All CTIs increase the interfacial tension between C-S-H and water, but the Bola-type topology consistently outperforms traditional straight-chain structures. Molecular dynamics simulations offer a reliable way to evaluate nanoscale IFT, circumventing experimental challenges.
(2) The repulsive interactions between the two head groups of Bola molecules promote a uniform distribution on the C-S-H surface and reduce self-aggregation. This maximizes the hydrophobic coverage area, enhancing suppression of transportation. Head groups must balance adsorption strength: strong enough to maintain attachment, but not so strong that they override repulsive interactions and increase aggregation, which would reduce surface coverage.
(3) -PO_3^{2-} exhibits sufficient adsorption strength and stability, and the Bola-type topology ensures low self-aggregation, allowing uniform surface distribution and effective transportation suppression. These characteristics make B-PO_3^{2-} the optimal molecular structure.

Overall, this work provides a new perspective for understanding CTI mechanisms in concrete systems. Future efforts could focus on synthesizing these molecules and exploring more complex systems, offering a powerful approach to observe and characterize CTIs at the microscopic level. Such studies will also support theoretical and experimental evaluation of performance in diverse concrete environments.

CRediT authorship contribution statement

Chengbo Liu: Writing – original draft, Validation, Methodology, Data curation. **Muhan Wang:** Writing – review & editing, Methodology, Investigation, Formal analysis, Conceptualization. **Cong Lu:** Writing – review & editing. **Xiangming Zhou:** Writing – review & editing, Supervision, Methodology, Formal analysis, Conceptualization. **Xinpeng Wang:** Writing – review & editing. **Dongshuai Hou:** Writing – review & editing. **Yue Zhang:** Writing – review & editing. **Qiuju Li:** Data curation. **Pan Wang:** Writing – review & editing.

Declaration of Competing Interest

The following are the author's contributions to this manuscript: Chengbo Liu: Experiments, Simulation, Data curation, Writing-Original draft. Qiuju Li: Data curation. Pan Wang, Yue Zhang, Xinpeng Wang, Dongshuai Hou, Cong Lu: Writing-Revising. Xiangming Zhou, Muhan Wang: Supervision, Conceptualization, Methodology, Writing-Revising.

All authors of this manuscript have reviewed the manuscript and approved it for publication.

Acknowledgment

M. W. and D. H. financial support from the National key research and development project 2022YFE0133800, the National Natural science foundation of China under Grant U2006224, 52308263, Shandong Province Natural Science Foundation under Grant ZR2022YQ55, Shandong Provincial Education Department under Grant 2023KJ320, Qingdao Research Program 16–5–1–96-jch, 111 Project TMduracon20220022. Newton International Fellowship NIF\R1\242498.

Data availability

The authors do not have permission to share data.

References

[1] S.W. Tang, Y. Yao, C. Andrade, Z.J. Li, Recent durability studies on concrete structure, Cem. Concr. Res 78 (2015) 143–154.
[2] M. Amiri, F. Hatami, E.M. Golafshani, Evaluating the synergic effect of waste rubber powder and recycled concrete aggregate on mechanical properties and durability of concrete, Case Stud. Constr. Mater. 15 (2021) e00639.
[3] Z. Li, X. Zhou, H. Ma, D. Hou, Advanced concrete technology, John Wiley & Sons, 2022.
[4] Y. Yi, D. Zhu, S. Guo, Z. Zhang, C. Shi, A review on the deterioration and approaches to enhance the durability of concrete in the marine environment, Cem. Concr. Compos 113 (2020) 103695.
[5] A.K. Akhnoukh, C. Buckhalter, Ultra-high-performance concrete: constituents, mechanical properties, applications and current challenges, Case Stud. Constr. Mater. 15 (2021) e00559.
[6] A. Younis, U. Ebead, S. Judd, Life cycle cost analysis of structural concrete using seawater, recycled concrete aggregate, and GFRP reinforcement, Constr. Build. Mater. 175 (2018) 152–160.

[7] X. Shi, N. Xie, K. Fortune, J. Gong, Durability of steel reinforced concrete in chloride environments: an overview, Constr. Build. Mater. 30 (2012) 125–138.
[8] A. Delagrave, M. Pigeon, J. Marchand, É. Revertégat, Influence of chloride ions and ph level on the durability of high performance cement pastes (part II), Cem. Concr. Res 26 (1996) 749–760.
[9] M. Wang, S. Yu, C. Liu, P. Wang, Y. Zhang, X. Wang, D. Hou, Design of high chloride-resistant passivation films: from synthesis to the mechanisms of nano-generation, Corros. Sci. 244 (2025) 112656.
[10] C. Wen, Y. Tian, Z. Mai, J. Hu, G. Wang, Effect of macropores at the steel-concrete interface on localized corrosion behaviour of steel reinforcement, Cem. Concr. Compos 129 (2022) 104510.
[11] Q. Li, W. Zhang, W. Shao, D. Shi, Numerical modeling of non-uniform corrosion of concrete reinforcement considering calcium leaching and chloride diffusion coupling effect, Corros. Sci. 237 (2024) 112343.
[12] S.P. Zhang, L. Zong, Evaluation of relationship between water absorption and durability of concrete materials, Adv. Mater. Sci. Eng. 2014 (2014) 650373.
[13] J. Zuquan, Z. Xia, Z. Tiejun, L. Jianqing, Chloride ions transportation behavior and binding capacity of concrete exposed to different marine corrosion zones, Constr. Build. Mater. 177 (2018) 170–183.
[14] J.G. Jang, H.-K. Lee, Microstructural densification and CO2 uptake promoted by the carbonation curing of belite-rich portland cement, Cem. Concr. Res 82 (2016) 50–57.
[15] K. Abora, I. Beleña, S.A. Bernal, A. Dunster, P.A. Nixon, J.L. Provis, A. Tagnit-Hamou, F. Winnefeld, Durability and testing–Chemical matrix degradation processes, in: Alkali Activated Materials: State-of-the-Art Report, RILEM TC 224-AAM, Springer, 2013, pp. 177–221.
[16] M. Butler, V. Mechtcherine, S. Hempel, Durability of textile reinforced concrete made with AR glass fibre: effect of the matrix composition, Mater. Struct. 43 (2010) 1351–1368.
[17] T. Xie, T. Ozbakkaloglu, Behavior of low-calcium Fly and bottom ash-based geopolymer concrete cured at ambient temperature, Ceram. Int 41 (2015) 5945–5958.
[18] Q. Song, Y. Yang, S. Xu, C. Liu, J. Liu, J. Bao, S. Xue, Mechanical properties, durability, and carbon emissions of concrete with coal gangue coarse aggregate, fine aggregate and mineral admixtures in coal mining environment, Case Stud. Constr. Mater. (2025) e05187.
[19] C. Chen, X. Zhang, Z. Cai, R. Liu, P. Zhu, X. Yan, J. Yu, J. He, Synergistic mechanism of the performance and recyclability of recycled fine aggregate concrete under chloride salt dry-wet cycles by composite mineral admixtures, Constr. Build. Mater. 491 (2025) 142683.
[20] Y. Wei, Z. Cao, J. Hou, B. Li, G. Jia, P. Chen, P. Liu, Study on the chloride ion binding rate of sulfoaluminate cement mortars containing different mineral admixtures, Sci. Rep. 14 (2024) 24277.
[21] M.H.F. Medeiros, P. Helene, Surface treatment of reinforced concrete in marine environment: influence on chloride diffusion coefficient and capillary water absorption, Constr. Build. Mater. 23 (2009) 1476–1484.
[22] H. Bi, W. Zhang, X. Xu, A. Ming, Y. Shen, S. Wang, X. Cheng, Chloride binding and transport characteristic of phosphoaluminate cement-based marine sand coating subjected to marine environment, Constr. Build. Mater. 281 (2021) 122505.
[23] T. Li, Y. Wu, H. Wu, A study on impact of different surface treatment agents on the durability of airport pavement concrete, Coatings 12 (2022) 162.
[24] V. Bouteiller, C. Cremona, V. Baroghel-Bouny, A. Maloula, Corrosion initiation of reinforced concretes based on portland or GGBS cements: chloride contents and electrochemical characterizations versus time, Cem. Concr. Res 42 (2012) 1456–1467.
[25] Y. Tissier, V. Bouteiller, E. Marie-Victoire, S. Joiret, T. Chaussadent, Y. Tong, Electrochemical chloride extraction to repair combined carbonated and chloride contaminated reinforced concrete, Electro Acta 317 (2019) 486–493.
[26] Y. Bai, P.A.M. Basheer, Influence of furnace bottom ash on properties of concrete, Proc. Inst. Civ. Eng. Struct. Build. 156 (2003) 85–92.
[27] Y. Liang, J. Wang, Experimental study on the application of limestone mine dust filter slag as concrete admixture, Materials 18 (2025) 3970.
[28] T.F. Awolusi, A.O. Sojobi, D.O. Oguntayo, O.O. Akinkurolere, B.O. Orogbade, Effects of calcined clay, sawdust ash and chemical admixtures on strength and properties of concrete for pavement and flooring applications using taguchi approach, Case Stud. Constr. Mater. 15 (2021) e00568.
[29] G. Lai, X. Liu, S. Li, Y. Xu, Y. Zheng, J. Guan, R. Gao, Z. Wei, Z. Wang, S. Cui, Development of chemical admixtures for Green and environmentally friendly concrete: a review, J. Clean. Prod. 389 (2023) 136116.
[30] H.F. Mahmood, H. Dabbagh, A.A. Mohammed, Comparative study on using chemical and natural admixtures (grape and mulberry extracts) for concrete, Case Stud. Constr. Mater. 15 (2021) e00699.
[31] A. Goyal, E. Ganjian, H.S. Pouya, M. Tyrer, Inhibitor efficiency of migratory corrosion inhibitors to reduce corrosion in reinforced concrete exposed to high chloride environment, Constr. Build. Mater. 303 (2021) 124461.
[32] Y. Gao, J. Li, Z. Lu, M. Zhang, L. Duan, J. Wang, Utilization of composite supplementary cementitious material containing circulating fluidized bed ash in concrete, Constr. Build. Mater. 479 (2025) 141486.
[33] M. Wang, H. Sun, X. Zhou, P. Wang, Z. Li, D. Hou, Surface engineering of migratory corrosion inhibitors: controlling the wettability of calcium silicate hydrate in the nanoscale, Langmuir 39 (2023) 17110–17121, https://doi.org/10.1021/acs.langmuir.3c01953.
[34] J. Huang, R. Chen, Y. Zhou, J. Ming, J. Liu, Molecular design and experiment of ion transport inhibitors towards concrete sustainability, Cem. Concr. Compos 133 (2022) 104710.
[35] D. Hou, L. Gao, P. Wang, Y. Zhou, J. Cai, W. Zhang, J. Zhang, The optimal design on the molecular structure of a fluid transport inhibitor applied to reinforced concrete structures, ACS Omega 6 (2021) 29692–29702.
[36] D. Hou, L. Gao, D. Chen, P. Wang, J. Wang, Y. Zhou, J. Zhang, Molecular-scale insights on structure-efficiency relationship of silane-based waterproofing agents, Constr. Build. Mater. 327 (2022) 126985.
[37] C. Liu, Y. Wang, Q. Liu, P. Wang, Y. Zhang, X. Wang, D. Hou, F. Xu, M. Wang, Topological effects on the concrete transportation inhibitors: Nano-mechanisms and design principles, Case Stud. Constr. Mater. 22 (2025), https://doi.org/10.1016/j.cscm.2025.e04560.
[38] Q. Liu, C. Liu, M. Wang, X. Ji, F. Hong, D. Hou, J. Zhang, M. Wang, Advancing understanding of polymer-based superplasticizers for diverse concrete applications: insights from quantum chemistry and nanoscale adsorption behavior, Cem. Concr. Compos 153 (2024) 105690.
[39] Y. Yang, Y. Tan, Z. Li, G. Zhou, X. Yu, D. Xu, Q. Yong, H. Zhao, Z. Xie, Interaction mechanisms between polycarboxylate superplasticizers and cement, and the influence of functional groups on superplasticizer performance: a review, Polym. Bull. 81 (2024) 10415–10438.
[40] X. Ji, C. Liu, Q. Liu, F. Hong, D. Hou, M. Wang, Molecular scale study on polyphosphate superplasticizers for cement fluidity improvement: impact of phosphorus-containing functional groups, Mater. Struct. 58 (2025) 1–16.
[41] R. Klinger, C. Kolářik, J. Fluck, M. Hofmann-Apitius, C.M. Friedrich, Detection of IUPAC and IUPAC-like chemical names, Bioinformatics 24 (2008) i268–i276.
[42] R.J.-M. Pellenq, A. Kushima, R. Shahsavari, K.J. Van Vliet, M.J. Buehler, S. Yip, F.-J. Ulm, A realistic molecular model of cement hydrates, Proc. Natl. Acad. Sci. 106 (2009) 16102–16107.
[43] H. Manzano, S. Moeini, F. Marinelli, A.C.T. Van Duin, F.-J. Ulm, R.J.-M. Pellenq, Confined water dissociation in microporous defective silicates: mechanism, dipole distribution, and impact on substrate properties, J. Am. Chem. Soc. 134 (2012) 2208–2215.
[44] S.J. Murray, V.J. Subramani, R.P. Selvam, K.D. Hall, Molecular dynamics to understand the mechanical behavior of cement paste, Transp. Res Rec. 2142 (2010) 75–82.
[45] N. Giraudo, S. Bergdolt, F. Laye, P. Krolla, J. Lahann, P. Thissen, Dehydration and dehydroxylation of C-S-H phases synthesized on silicon wafers, Appl. Surf. Sci. 433 (2018) 589–595.
[46] J.W. Ponder, D.A. Case, Force fields for protein simulations, Adv. Protein Chem. 66 (2003) 27–85.
[47] F. Hong, M. Wang, B. Dong, X. Diao, X. Zhang, K. Pang, Y. Zhang, D. Hou, Molecular insight into the pozzolanic reaction of metakaolin and calcium hydroxide, Langmuir 39 (2023) 3601–3609.
[48] F. Hong, C. Liu, M. Wang, X. Ji, M. Wang, Z. Li, D. Hou, M. Li, Molecular dynamics study of surface alkalization reaction in high calcium systems, J. Build. Eng. 91 (2024) 109475.
[49] S.W.I. Siu, K. Pluhackova, R.A. Böckmann, Optimization of the OPLS-AA force field for long hydrocarbons, J. Chem. Theory Comput. 8 (2012) 1459–1470.

[50] W.L. Jorgensen, J. Tirado-Rives, The OPLS [optimized potentials for liquid simulations] potential functions for proteins, energy minimizations for crystals of cyclic peptides and crambin, J. Am. Chem. Soc. 110 (1988) 1657–1666.
[51] A.P. Thompson, H.M. Aktulga, R. Berger, D.S. Bolintineanu, W.M. Brown, P.S. Crozier, P.J. In't Veld, A. Kohlmeyer, S.G. Moore, T.D. Nguyen, others, LAMMPS-a flexible simulation tool for particle-based materials modeling at the atomic, meso, and continuum scales, Comput. Phys. Commun. 271 (2022) 108171.
[52] D.J. Evans, B.L. Holian, The nose–hoover thermostat, A)'=(A Is.) 1 (1985) 18.
[53] P.A.M. Dirac, Generalized Hamiltonian dynamics, Proc. R. Soc. Lond. A Math. Phys. Sci. 246 (1958) 326–332.
[54] S.H. [Ubar], I. NOSÉ, A molecular dynamics method for simulations in the canonical ensemble, Mol. Phys. 100 (2002) 191–198.
[55] G.M. Torrie, J.P. Valleau, Nonphysical sampling distributions in Monte Carlo free-energy estimation: umbrella sampling, J. Comput. Phys. 23 (1977) 187–199.
[56] Y. Mitsuta, T. Asada, Parameter optimization method in multidimensional umbrella sampling, J. Chem. Theory Comput. 20 (2024) 6531–6548.
[57] J.S. Hub, B.L. De Groot, D. Van Der Spoel, g_wham-A free weighted histogram analysis implementation including robust error and autocorrelation estimates, J. Chem. Theory Comput. 6 (2010) 3713–3720.
[58] M. Souaille, B. Roux, Extension to the weighted histogram analysis method: combining umbrella sampling with free energy calculations, Comput. Phys. Commun. 135 (2001) 40–57.
[59] T.D. Kühne, M. Iannuzzi, M. Del Ben, V.V. Rybkin, P. Seewald, F. Stein, T. Laino, R.Z. Khaliullin, O. Schütt, F. Schiffmann, others, CP2K: an electronic structure and molecular dynamics software package-Quickstep: efficient and accurate electronic structure calculations, J. Chem. Phys. 152 (2020).
[60] C.S. Ahart, K.M. Rosso, J. Blumberger, Implementation and validation of constrained density functional theory forces in the CP2K package, J. Chem. Theory Comput. 18 (2022) 4438–4446.
[61] C. Guerra, J. Burgos, L. Ayarde-Henr\'\iquez, E. Chamorro, Formulating reduced density gradient approaches for noncovalent interactions, J. Phys. Chem. A 128 (2024) 6158–6166.
[62] A. Savin, R. Nesper, S. Wengert, T.F. Fässler, ELF: the electron localization function, Angew. Chem. Int. Ed. Engl. 36 (1997) 1808–1832.
[63] T. Lu, F. Chen, Multiwfn: a multifunctional wavefunction analyzer, J. Comput. Chem. 33 (2012) 580–592.
[64] J.D. Berry, M.J. Neeson, R.R. Dagastine, D.Y.C. Chan, R.F. Tabor, Measurement of surface and interfacial tension using pendant drop tensiometry, J. Colloid Interface Sci. 454 (2015) 226–237.
[65] T. Passot, E. Vázquez-Semadeni, Density probability distribution in one-dimensional polytropic gas dynamics, Phys. Rev. E 58 (1998) 4501.
[66] S. Park, K. Schulten, Calculating potentials of mean force from steered molecular dynamics simulations, J. Chem. Phys. 120 (2004) 5946–5961.
[67] M. Rovere, D.W. Hermann, K. Binder, Block density distribution function analysis of two-dimensional Lennard-Jones fluids, Eur. Lett. 6 (1988) 585.
[68] A.P. Lyubartsev, A. Laaksonen, Calculation of effective interaction potentials from radial distribution functions: a reverse Monte Carlo approach, Phys. Rev. E 52 (1995) 3730.
[69] G.D. Harp, B.J. Berne, Time-correlation functions, memory functions, and molecular dynamics, Phys. Rev. A (Coll. Park) 2 (1970) 975.
[70] K. Sargsyan, C. Grauffel, C. Lim, How molecular size impacts RMSD applications in molecular dynamics simulations, J. Chem. Theory Comput. 13 (2017) 1518–1524.
[71] O. Carugo, How root-mean-square distance (rmsd) values depend on the resolution of protein structures that are compared, Appl. Crystallogr. 36 (2003) 125–128.